

Numerical visualization of wind turbine wakes using passive scalar advection–diffusion equation and its application for wake management

Wind Engineering
2022, Vol. 46(6) 1870–1887
© The Author(s) 2022
Article reuse guidelines:
sagepub.com/journals-permissions
DOI: 10.1177/0309524X221113011
journals.sagepub.com/home/wie


Takanori Uchida¹ , Susumu Takakuwa² , Keiichiro Watanabe²,
Seiya Hasegawa², Yoshitaka Baba³, Reo Murakami³,
Masahide Yamasaki³ and Kunihiko Hidaka³

Abstract

To visualize and characterize the unsteady properties of the wake trailing behind a wind turbine, we propose a novel numerical methodology in this study. Through a wind-tunnel experiment using a smoke generator, we succeeded in visualizing a compact-type small-scale wind turbine wake using continuous scalar plumes from a single point source. Next, to simulate the above wind-tunnel experiment, we proposed a method using the passive scalar advection–diffusion equation based on a high-fidelity large-eddy simulation (LES). The actuator-line method (ALM) was adopted for the wind turbine model. We succeeded in qualitatively reproducing the wake visualization experiment in the wind tunnel described above and verified the effectiveness of the proposed numerical visualization method. To evaluate the characteristics of wakes generated by wind turbines in more detail, we conducted a quantitative comparison using a disk-shaped volume source with the same size as the swept area, set behind the wind turbine model. The results indicated that the non-dimensional time-averaged passive scalar profile in the near- and far-wake regions qualitatively matched the shape of the streamwise velocity profile, despite having opposite signs. In other words, it was shown that if a disk-shaped volume source with the same size as the swept area is placed just behind the wind turbine, it is possible to accurately predict the behavior of the wind turbine wake. Finally, to validate the proposed method for wind farm wake management, we performed a visualization of wake flows in a virtual offshore wind farm consisting of 12 wind turbines with short separation distances. Through detailed comparison of two types of numerical results with different wind directions, we showed that the proposed method can effectively demonstrate the range of spatial influence of the wakes formed by the wind turbine with special attention.

Keywords

Wind turbine wakes, wind tunnel experiment, large-eddy simulation (LES), passive scalar advection–diffusion equation, flow visualization, large offshore wind farm, wake management

Introduction

Wind turbines extract energy from the wind and cast a wind shadow in the downstream direction. Specifically, wind turbines reduce the wind speed behind the rotor while, at the same time, forming a swirling flow. The flows behind turbines are called “wakes” (Porté-Agel et al., 2020). According to past review articles (Sanderse et al., 2011; Vermeer et al., 2003) concerning wind turbine wake aerodynamics, the wakes are divided into two regions. One is the near-wake region, within 1–5 rotor diameters (D) behind the turbine. In the near-wake region, the three-dimensional flow structure is complex due to the rotor properties and various operations (e.g. yaw and pitch angle

¹Research Institute for Applied Mechanics (RIAM), Kyushu University, Kasuga, Fukuoka, Japan

²Japan Renewable Energy Corporation, Tokyo, Japan

³Tokyo Gas Co., Ltd., Tokyo, Japan

Corresponding author:

Takanori Uchida, Research Institute for Applied Mechanics (RIAM), Kyushu University, 6-1 Kasuga-kouen, Kasuga, Fukuoka 816-8580, Japan.

Email: takanori@riam.kyushu-u.ac.jp

control in wind turbine). As a result, the flow field in the near-wake region is dominated by turbine-generated coherent turbulent structures, such as strong blade tip vortices, hub vortices, and tower vortices. Among these vortex structures, blade tip vortices are known to form the spiral structure in the downstream of the wind turbine. The other region is the far-wake region, which lies beyond the near-wake region. In the far-wake region, the influence of rotor properties is less important. It has been reported that the interactions of the aforementioned vortex structures in the near-wake region directly affect the evolution and turbulent flow characteristics in the far-wake region (Sørensen, 2011).

Forming locally concentrated groups by clustering wind turbines in large offshore wind farms provides the benefit of being geographically limited while maintaining profitable wind resources. As a result, clustering wind turbines has also been reported to reduce the overall costs associated with wind turbine maintenance. However, despite the design innovation and development of locally clustered wind turbines, several drawbacks have also been associated with wind-turbine wakes and their mutual interference. First of all, the significant deficit in wind speeds, due to the extraction of kinetic energy in the wind by upstream wind turbines, results in dramatically lower power production in turbines located downstream. Furthermore, the increases in local turbulence in the wake regions create significant unsteady fatigue loads on the downstream turbines, which can shorten their working life.

To better understand the nature and vulnerabilities of wake flows and their mutual interactions, we first need to study their characteristics when generated by a single wind turbine without external interference. The operation and maintenance (O&M) of wind farms, if based on a more comprehensive knowledge and understanding of flow physics, could promote the development of cost-effective offshore wind farms and provide insight into whether certain large-scale operations could be financially viable. Establishing a novel methodology for turbine wake visualization could play an important role in reducing wake losses and negative structural impacts in the development of future wind farms (Emeis, 2010; Hasager et al., 2017). Emeis (2010) has examined familiar wake photographs taken on 12 February 2008 at the offshore Horns Rev 1 wind farm, and offered detailed meteorological explanation of the wake clouds. Hasager et al. (2017) have also investigated the same wake photographs from a helicopter, using a combination of satellite data, local meteorological observations, and radio-sounding data, as well as supervisory control and data acquisition (SCADA) data. The special atmospheric conditions were described and an interpretation of the origin of the fog was provided. Furthermore, advanced wake modeling with computational fluid dynamics (CFD) using a detached eddy simulation (DES) of a full wind turbine rotor allowed for determination of the details of the physical processes (e.g. mechanically driven convection processes) in the wakes of the wind turbines, in relation to the formation and the dispersion of fog. As a result, the above research and development may lead to advanced yaw-based wake steering, a form of modern offshore wind-farm control, where upstream turbines operate with yaw misalignment to deflect their wakes away from downstream turbines, yielding a net power gain for the wind plant (Houck, 2022).

In the present study, we propose an experimental and numerical methodology to visualize and characterize the unsteady aerodynamics of wakes trailing behind wind turbines, specifically visualizing high-fidelity large eddy simulation (LES) data using the passive scalar advection–diffusion equations. The proposed method is based on the actuator-line concept, as the wind turbine model. With a view to applying the proposed method to wake management, we conducted visualization of wake flows using a virtual offshore wind farm consisting of 12 wind turbines, and clarified the spatial range affected by the wake effects.

Motivation and idea of wind turbine wake visualization

As shown in Figure 1, wind turbine wake-effect visualization plays an important role in reducing the total O&M costs of future wind farms (Emeis, 2010; Hasager et al., 2017). As a result, the research and development that has been conducted may lead to advanced yaw-based wake-steering strategies for wind farms, in order to optimize their energy production and fatigue loads. Figure 2 shows a photograph that inspired our numerical wake-visualization method. There is a point that I would like you to pay close attention to here. That is, this photo shows the smoke emanating from the wind turbine due to a nacelle fire. To verify the validity of our proposed method, we conducted a wind-tunnel experiment by adding smoke to the air passing through our wind turbine model.

Description of experimental equipment (boundary-layer wind tunnel)

Wind tunnels can be classified into two main types: Open- and closed-circuit. In an open-circuit tunnel, the airflow follows a straight path from the entrance, through a contraction zone to the test section; then, it moves into a diffuser, a fan section, and an outlet. In a closed-circuit wind tunnel, the air recirculates continuously, with little or



Figure 1. Aerial view (photograph) of wake clouds at Horns Rev I offshore wind farm 12 February 2008 at around 10:10 UTC, as seen from the southeast.



Figure 2. Photograph that inspired our numerical wake visualization method (https://www.meti.go.jp/shingikai/sankoshin/hoan_shohi/denryoku_anzen/newenergy_hatsuden_wg/pdf/012_02_00.pdf).

no exchange with the outside. The wind tunnel facility used in this study was a closed-circuit boundary-layer wind tunnel (test section: 15 m long \times 3.6 m wide \times 2.0 m high) at the Research Institute for Applied Mechanics (RIAM) of Kyushu University, as shown in Figure 3. Figure 3a presents an overall view of the facility, whereas Figure 3b presents an enlarged view of the test section and the sidewall of the wind tunnel. Notably, Richmond-Navarro et al. (2022) have studied the shrouded wind turbine performance in yawed turbulent-flow conditions at the same facility.

Experimental set-up

We prepared two types of three-bladed, fixed-pitch, small-scale wind turbine models in the present wind tunnel experiment. Figure 4 shows a schematic view of the torque measurement system used in the performance test of the small-scale wind turbine model that we produced. Figure 4a specifies the various parameters in the performance test. The inflow wind speed (U_{in}) was set to 12 m/s in the wind tunnel experiment. We did not consider the scaled boundary layer, which is typically created in the wind tunnel using triangular spires and distributed roughness elements. For this study, we set a uniform flow, in which the wind speed did not change in the height direction. The hub height of the wind turbine model used in this study was 1 m, and the rotor diameter was 0.442 m. The Reynolds number $Re = U_{in} D/\nu$, determined for a rotor diameter D of 0.442 m, was on the order of 10^5 , where ν is the kinematic viscosity of the fluid. The voltage output of the wind turbine model was low-pass filtered at 1 Hz and recorded at 1 kHz for 30 seconds, then subsequently averaged based on 30,000 voltage output data.

Figure 4b shows photos of the small-scale wind turbine model produced for performance testing installed in the wind tunnel. Furthermore, the torque meter and servo motor used in this study are also shown in Figure 4b.

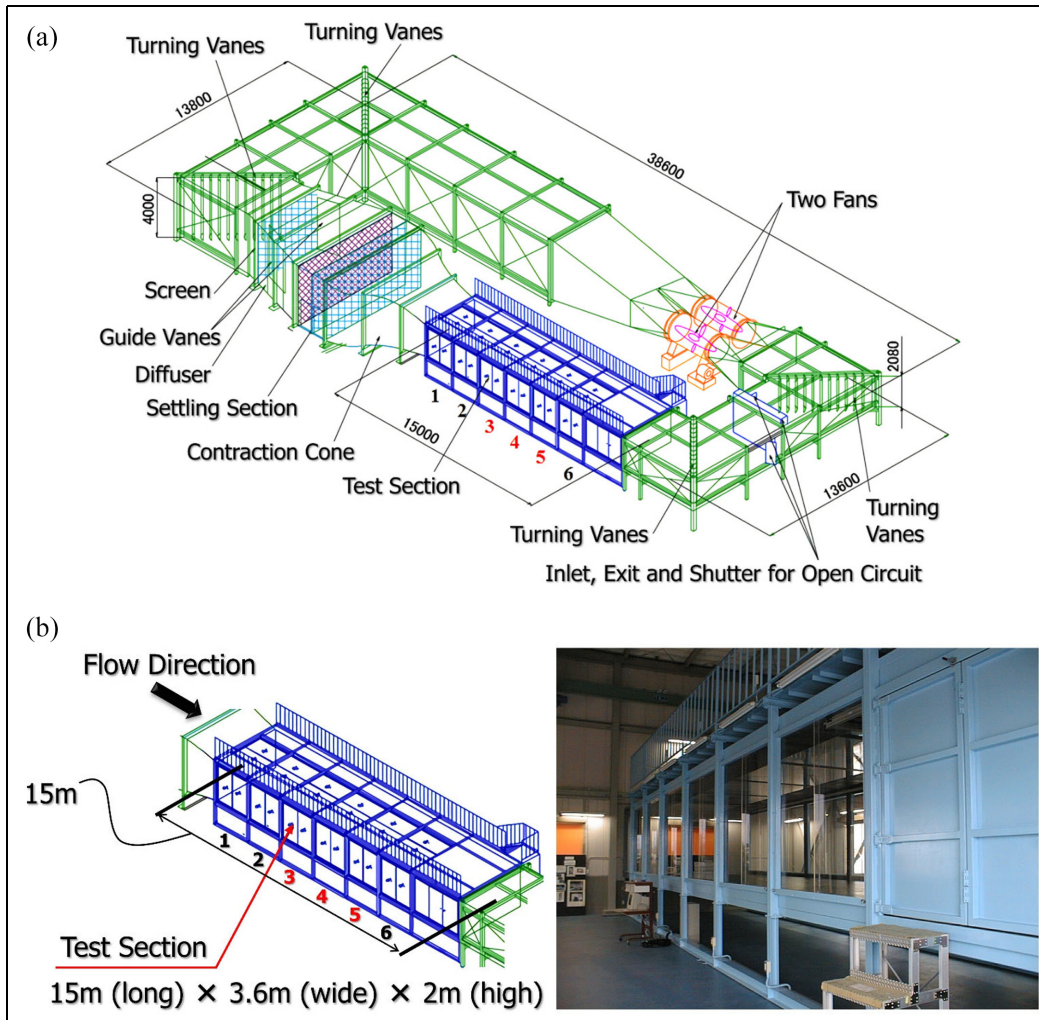


Figure 3. Closed-circuit wind tunnel facility used in this study: (a) perspective view and (b) enlarged view of the test section and photo of the sidewall of the wind tunnel.

Figure 5 shows cross-sections of the small-scale wind turbine blade at five typical radial positions from root to tip. The blades of the wind turbine model were based on the airfoils designed by Matsumiya et al. (2011). The gravity center position is also specified in this figure. Figure 6 shows the variation of the chord length (in red) and the twist angle (in blue) from the root to the tip of the blade, while Figure 7 shows the lift coefficient (C_l , red) and drag coefficient C_d (C_d , blue) against the angle of attack in the blade cross-section at the 75% position from the rotor center.

In order to carry out the wake-trailing visualization, we prepared a wind turbine model different from the model shown in Figure 4b. Here, for convenience, the model is called a compact-type small-scale wind turbine model and is shown in Figure 8. In this model, only the rotor rotation speed can be controlled. Figure 8a shows the perspective view, and Figure 8b shows the enlarged view. As shown in Figure 8b, there is no torque meter, as shown in Figure 4; only the same servo motor as shown in Figure 4 was stored in the box corresponding to the nacelle. The smoke generator (Model 8304, KANOMAX) shown in Figure 9 was used to visualize the three-dimensional wake trailing behavior. In order to guide the smoke from the smoke generator, a vinyl tube with a diameter of 1.8 cm was installed behind the nacelle box of the wind turbine scale model (see Figure 8b).

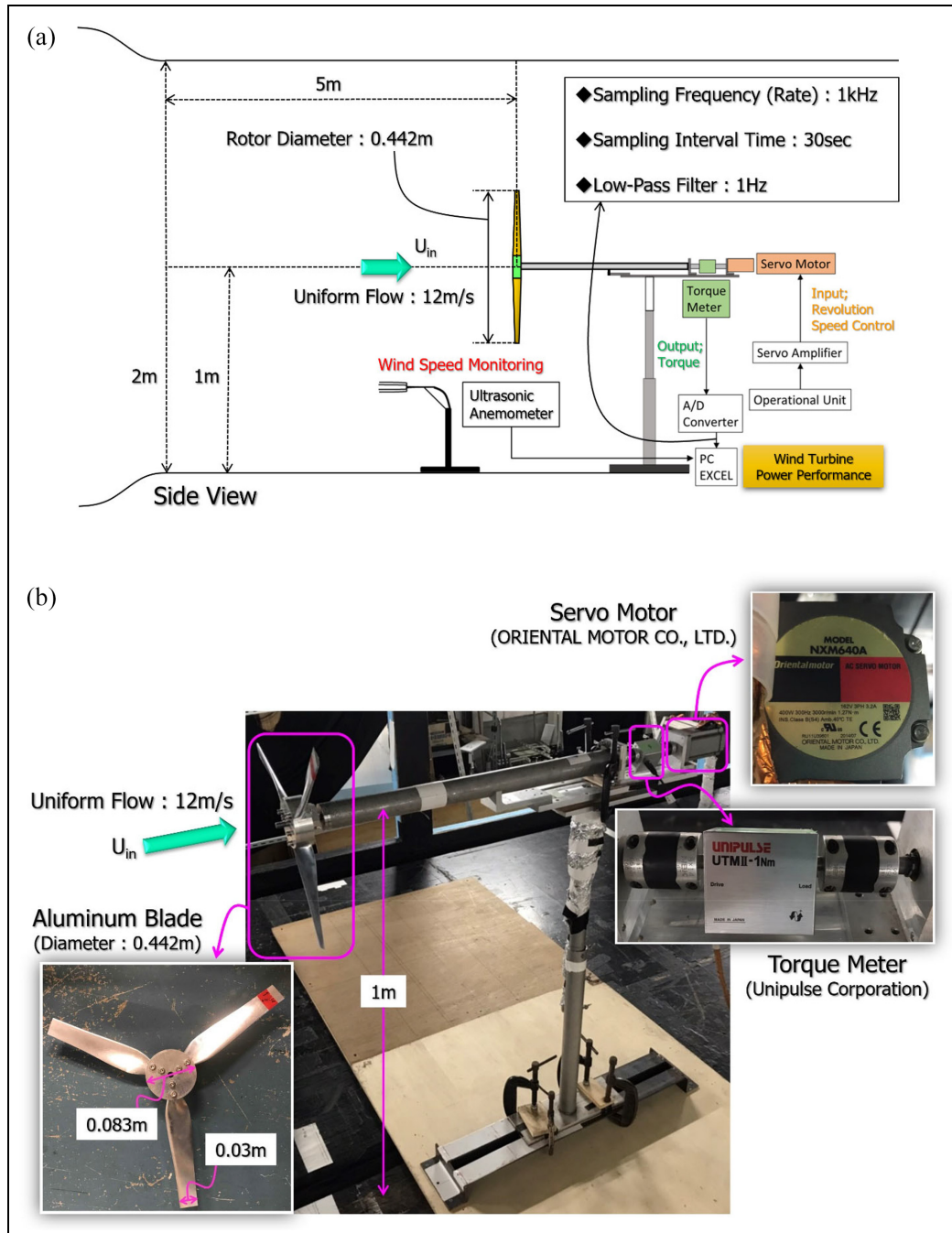


Figure 4. Schematic view of the torque measurement system used in the performance test: (a) various parameters in the performance test and (b) photos of the small-scale wind turbine model produced for performance testing.

Experimental results and discussions

Figure 10 shows the experimental results obtained by the torque measurement system used in this study (shown in Figure 4). The horizontal axis shows the tip-speed ratio (TSR), while the vertical axis shows the power coefficient (C_p). Figure 10 also shows the definition formulas for the TSR, C_p , and the variables used. These results confirmed that the design tip speed ratio (DTSR) of the small-scale wind turbine model used in this study was in the

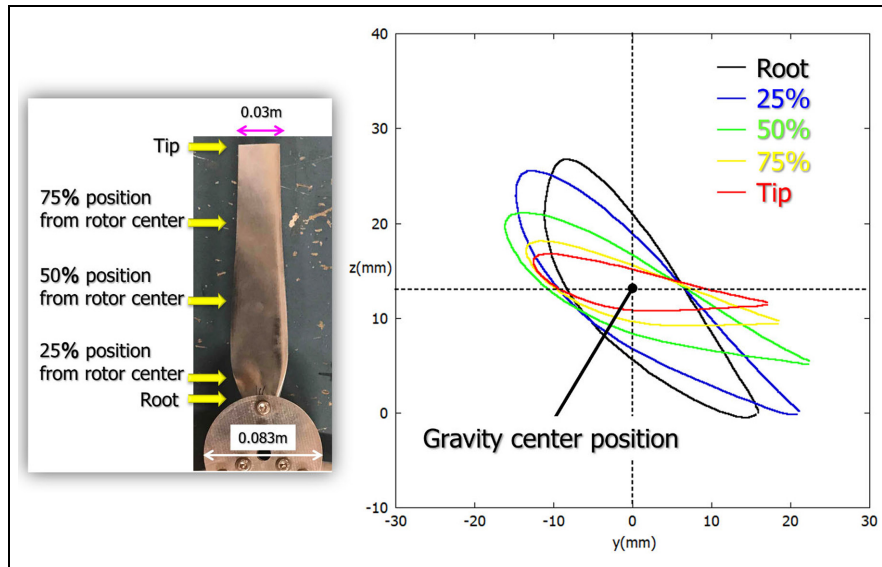


Figure 5. Cross-section of the wind turbine blade at typical radial position.

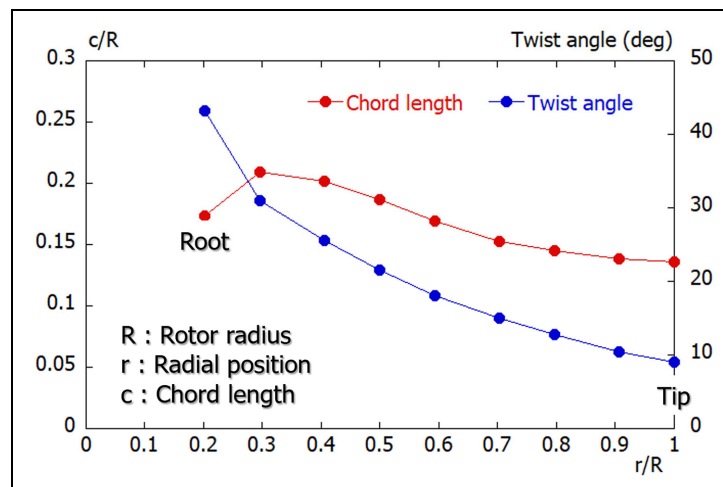


Figure 6. Variation of the chord length and the twist angle from the root to the tip of the blade.

vicinity of 4.0. The same figure also shows the numerical results of the DTSR obtained by the in-house LES-solver using the actuator-line method (ALM) (Porté-Agel et al., 2020). Comparing the wind-tunnel experiment and the LES results, it was found that the ALM implemented within the in-house LES-solver could accurately reproduce the performance of the small-scale wind turbine model.

Figure 11 shows the results of wind turbine wake-trailing visualization using the compact-type small-scale wind turbine model with a DTSR of 4.0. The wind speed was set to 1 m/s. The behavior of the smoke emitted from the back of the box, corresponding to the nacelle, revealed the wind turbine wake and its development (i.e. wake spreading).

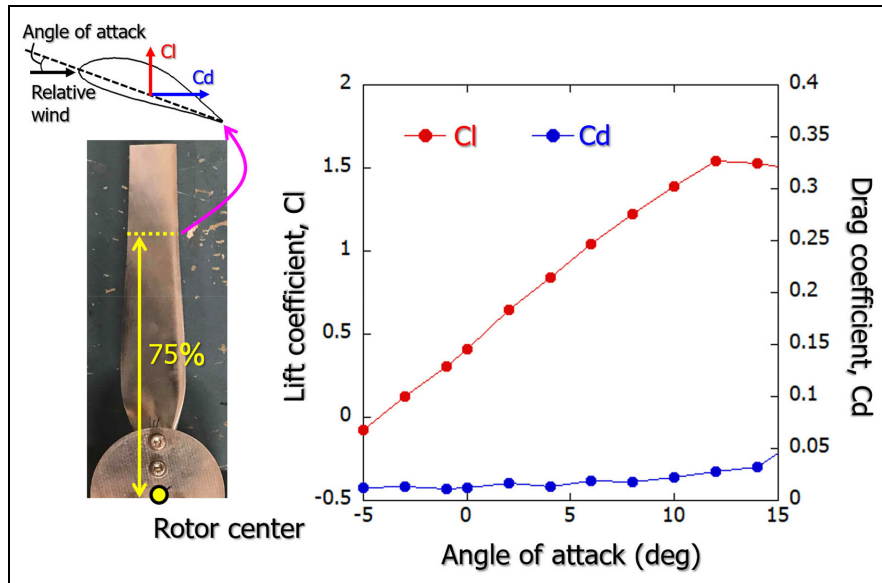


Figure 7. Lift and drag coefficients against angle of attack in the blade cross-section at the 75% position from the rotor center.

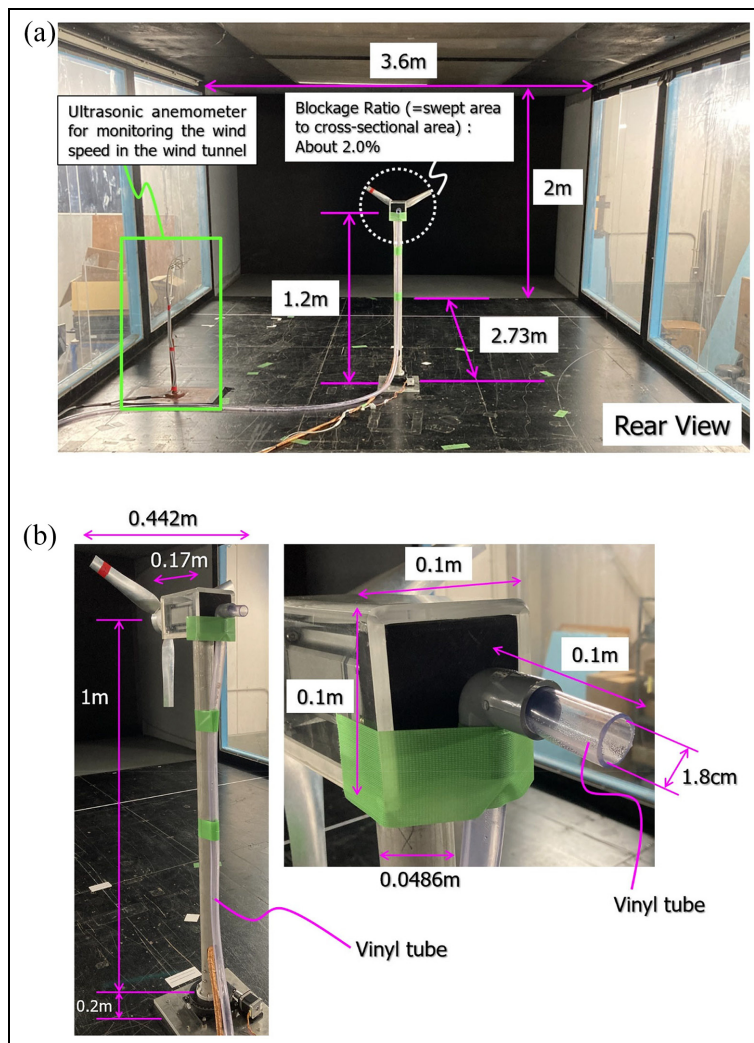


Figure 8. Compact-type small-scale wind turbine model for the wake-trail visualization experiment: (a) perspective view and (b) enlarged view.



Figure 9. Smoke generator used in this study.

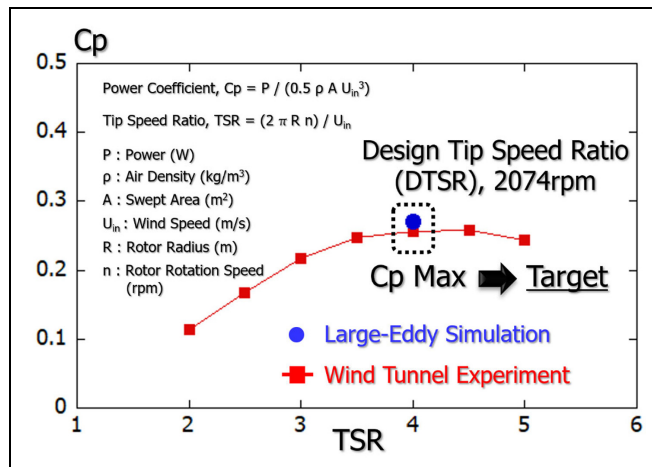


Figure 10. Relationship between the time-averaged tip speed ratio (TSR) and the power coefficient (Cp) of the small-scale wind turbine model produced for performance testing (shown in Figure 4).

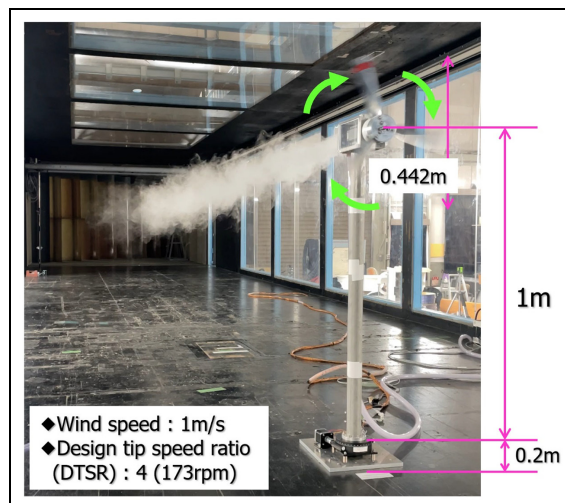


Figure 11. Wind turbine wake-trailing visualization results using the compact-type small-scale wind turbine model under the DTSR = 4.0.

Numerical design

The finite-difference method (FDM) based on a Cartesian grid system was adopted, and a large eddy simulation (LES) model was used for the turbulence model. In the LES model, a spatial filter was applied to the flow field to separate eddies at various scales into grid-scale (GS) components (which were larger than the computational grid cells) and sub-grid-scale (SGS) components (which were smaller than the computational grid cells). Large-scale eddies, including the GS components of turbulence eddies, were numerically simulated without the use of a simplified model. In contrast, the dissipation of energy, which is the main effect of small-scale eddies (i.e. the SGS components), was modeled according to a physics-based analysis of SGS stress.

For the governing equations of flow in tensor form ($i, j = 1, 2, 3$), a filtered continuity equation for an incompressible fluid (equation (1)) and a filtered Navier–Stokes equation (equation (2)) were used. In the current simulation, to visualize and characterize the unsteady properties of the wakes trailing behind the wind turbines, the standard passive scalar convection–diffusion equation (equation (3)) was solved by coupling it with equations (1) and (2) (Uchida and Araya, 2021). Re and Pr in equations (2) and (3) are the Reynolds number and Prandtl number ($= 0.71$), respectively.

For the computational algorithm, a method similar to the fractional-step (FS) method (Kim and Moin, 1985) was used, and a time-marching method based on the simplest explicit one-step method was adopted. Poisson's equation for pressure was solved using the successive over-relaxation (SOR) method. For the discretization of all spatial terms, except for the convective term in equations (2) and (3), a second-order central-difference scheme was applied. For the convective term, a third-order upwind-difference scheme was applied. The interpolation technique (Kajishima, 1994) was used for the fourth-order central differencing, which appeared in the discretized form of the convective term. For weighting of the numerical diffusion term in the convective term discretized by third-order upwind differencing, $\alpha = 0.5$ was used, as opposed to $\alpha = 3.0$ in the Kawamura–Kuwahara scheme (Kawamura et al., 1986), in order to minimize the influence of numerical diffusion. For LES sub-grid-scale modeling, the explicit mixed-timescale (MTS) model (Inagaki et al., 2005), based on an eddy-viscosity assumption, was adopted (equations (5)–(12)) for the turbulent flow field, and Simpson's rule was used as the test filter in the MTS procedure. Furthermore, an algebraic eddy-viscosity model (0-equation model) was also used for the passive scalar field (equations (13)–(15)). Here, we have summarized nomenclature into Appendix, so please refer to Appendix for details. For convenience, upper bars denoting application of the spatial filter will be omitted.

For the rotation of the wind turbine blades, an actuator-line method (ALM) was used to approximate the individual rotor blades, as lines of body force, without resolving all of the geometrical details and the boundary layer resolution of the wind turbine (Porté-Agel et al., 2020). In the ALM, the tangential and thrust forces generated by the rotating blade were added to the filtered Navier–Stokes equations (equation (2)), as external force terms representing the reaction forces exerted on the fluid in the direction of stream-wise flow and rotation. The force in the direction of rotation was decomposed into the spanwise and vertical directions. The ALM provided a realistic approximation of the wake structures with only the blade chord length, the lift coefficient, the drag coefficient, and the angle of attack (as a function of the distance from the center of the rotor) as inputs. Furthermore, the ALM significantly increased the computational speed, as compared to the fully resolved wind turbine CFD simulation including a moving mesh. In previous work, the in-house LES-solver and a Reynolds-averaged Navier–Stokes (RANS)-based commercial CFD software have been compared, where the in-house LES-solver provided comparable results to the RANS-based commercial software (Uchida and Li, 2018).

$$\frac{\partial \bar{u}_i}{\partial x_i} = 0 \quad (1)$$

$$\frac{\partial \bar{u}_i}{\partial t} + \bar{u}_j \frac{\partial \bar{u}_i}{\partial x_j} = -\frac{\partial \bar{p}}{\partial x_i} + \frac{1}{Re} \frac{\partial^2 \bar{u}_i}{\partial x_j \partial x_j} - \frac{\partial \tau_{ij}}{\partial x_j} \quad (2)$$

$$\frac{\partial \bar{c}}{\partial t} + \bar{u}_j \frac{\partial \bar{c}}{\partial x_j} = \frac{1}{Re Pr} \frac{\partial^2 \bar{c}}{\partial x_j \partial x_j} - \frac{\partial h_j}{\partial x_j} \quad (3)$$

$$\tau_{ij} \approx \overline{u'_i u'_j} \approx \frac{1}{3} \overline{u'_k u'_k} \delta_{ij} - 2\nu_{SGS} \bar{S}_{ij} \quad (4)$$

$$\nu_{SGS} = C_{MTS} k_{es} T_s \quad (5)$$

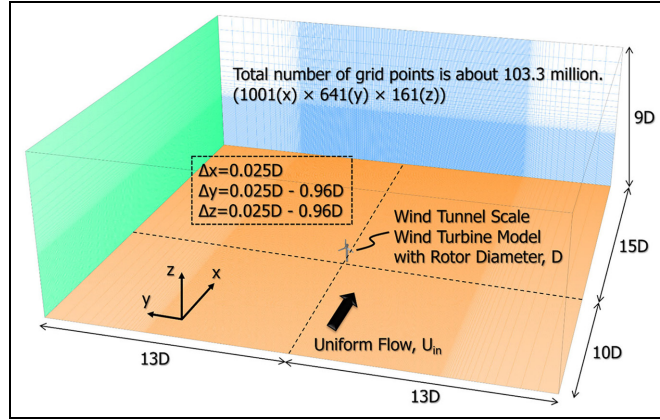


Figure 12. Computational domain, computational grid, coordinate system, and so on.

$$T_S^{-1} = \left(\frac{\Delta}{\sqrt{k_{es}}} \right)^{-1} + \left(\frac{C_T}{|\bar{S}_{ij}|} \right)^{-1} \quad (6)$$

$$k_{es} = (\bar{u}_k - \hat{u}_k)^2 \quad (7)$$

$$\bar{S}_{ij} = \frac{1}{2} \left(\frac{\partial u_i}{\partial x_j} + \frac{\partial u_j}{\partial x_i} \right) \quad (8)$$

$$|\bar{S}| = (2\bar{S}_{ij}\bar{S}_{ij})^{1/2} \quad (9)$$

$$\Delta = (\Delta_x \cdot \Delta_y \cdot \Delta_z)^{1/3} \quad (10)$$

$$C_{MTS} = 0.05 \quad (11)$$

$$C_T = 10.0 \quad (12)$$

$$h_j = -\alpha_{SGS} \frac{\partial \bar{c}}{\partial x_j} \quad (13)$$

$$\alpha_{SGS} = \frac{\nu_{SGS}}{Pr_{SGS}} \quad (14)$$

$$Pr_{SGS} = 0.5 \quad (15)$$

A computational domain was set very wide in order to carry out CFD simulation under the ideal case (blockage-free condition). Figure 12 shows a computational domain [25 D (x) × 26 D (y) × 9 D (z)], including the total number of grid points and the grid resolutions in the stream-wise and cross-stream directions, where D is the rotor diameter of the wind turbine model. The total number of grid points in the computational domain was approximately 103.3 million [1001 (x) × 641 (y) × 161 (z)]. The uniform spatial resolution in the stream-wise direction (Δx) was 0.025 D, and the non-uniform spatial resolution in the cross-stream directions (Δy and Δz) was in the range 0.025–0.96 D. To evaluate the influence of the rotating blades on the flow field, the ALM (based on blade-element theory) was applied. In order to reproduce the hub, nacelle and tower as objects, all of the velocity components were set to zero at all grid points on the surface and inside of the hub, nacelle and tower. Only a steady, uniform flow profile was used as an inlet boundary condition. The effects of shear and turbulence have already been discussed by the first author (Uchida, 2020). The lateral and upper boundary conditions were assigned as slip conditions, while the outflow section was assigned the Sommerfeld radiation condition (SRC). A no-slip boundary condition was set at the ground. The time step was $\Delta t = 1 \times 10^{-3}$ (R/ U_{in}), where U_{in} is the uniform flow speed and R is the radius of the wind turbine blade. To fully develop the flow field in both near- and far-wake regions downstream, time integration from $t = 0$ to 100 (R/ U_{in}) was performed. The flow-field statistical processing was performed at $t = 50$ –100 (R/ U_{in}) in the latter half of the time integration. The current LES

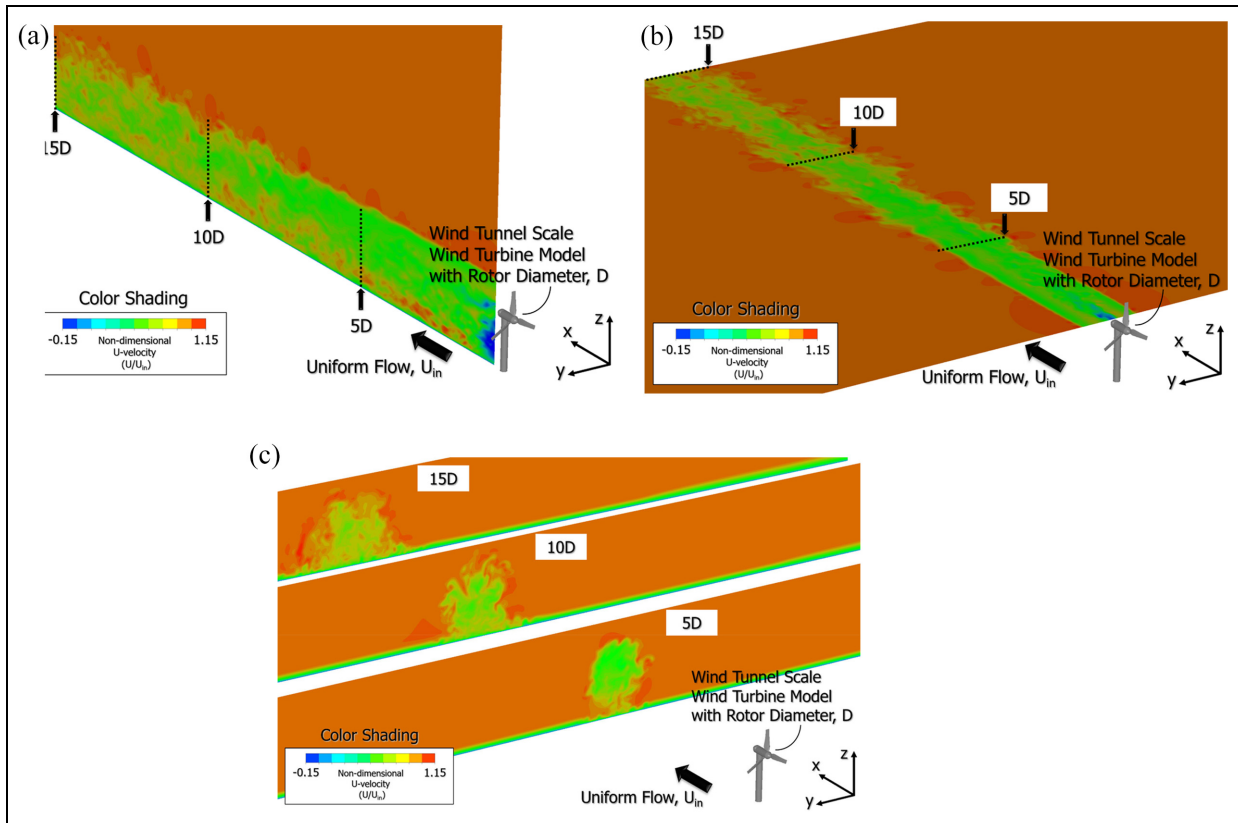


Figure 13. Color shading of non-dimensional instantaneous stream-wise velocity fields behind the compact-type small-scale wind turbine model under $DTSR = 4.0$: (a) x - z (side) plane, (b) x - y (top) plane, and (c) y - z (rear) planes.

simulations were performed using a new SX-Aurora TSUBASA vector supercomputer. The CPU time required for each simulation was several days.

Numerical results and discussions

First, let us consider the behavior of the wind turbine wake under $DTSR = 4.0$ (a constant rpm). For this purpose, Figure 13 shows the color shading of the non-dimensional instantaneous stream-wise velocity fields behind the wind turbine model. In the near-wake region (i.e. within 1–5 D behind the turbine), the three-dimensional flow structure was complex, due to the occurrence of various types of vortices (e.g. strong trailing tip vortices, hub vortices, and tower vortices) and their mutual interference. A strong velocity shear was formed near the wind turbine blade tip, due to the formation of strong helical tip vortices. As a result, the momentum exchange between the external flow and the wake flow was strongly suppressed. Therefore, the flow field in the near-wake region was dominated by turbine-generated coherent turbulent structures, such as strong helical tip vortices at the wind turbine blade tip, hub vortices, and tower vortices.

In the far-wake region (i.e. downstream of 5 D), the tip vortices gradually collapsed, resulting in the influence of rotor properties becoming less important. In this region, the wake flow was fully developed, and the velocity deficit and the additional turbulence intensity were assumed to be axisymmetric and to have self-similar distributions in the wake cross-sections (Porté-Agel et al., 2020). As mentioned earlier, in the present simulation, a time integration is performed up to $t = 100 (R/U_{in})$, we think that all physical quantities have converged within some standard. In the current simulation results, significant velocity deficits were found at even 15 D downstream, due to uniform inflow conditions without any terrain and inflow turbulence imposed.

To reproduce the smoke behavior continuously added to the wake region, as shown in Figures 8 and 11, the volume source was set behind the wind turbine model (see Figure 14). As mentioned in Section 6, the filtered Navier–Stokes equations coupled with the passive scalar transport were solved using LES. Figure 15 shows the

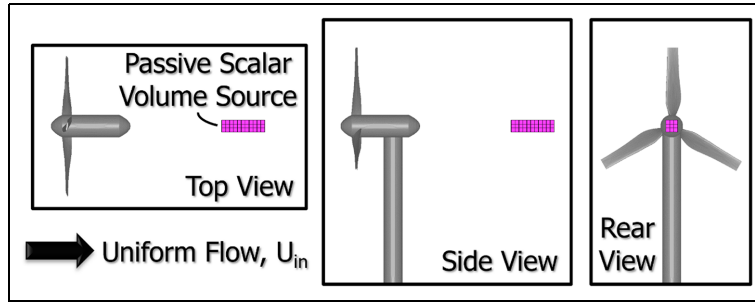


Figure 14. Small passive scalar volume source behind the compact-type small-scale wind turbine model.

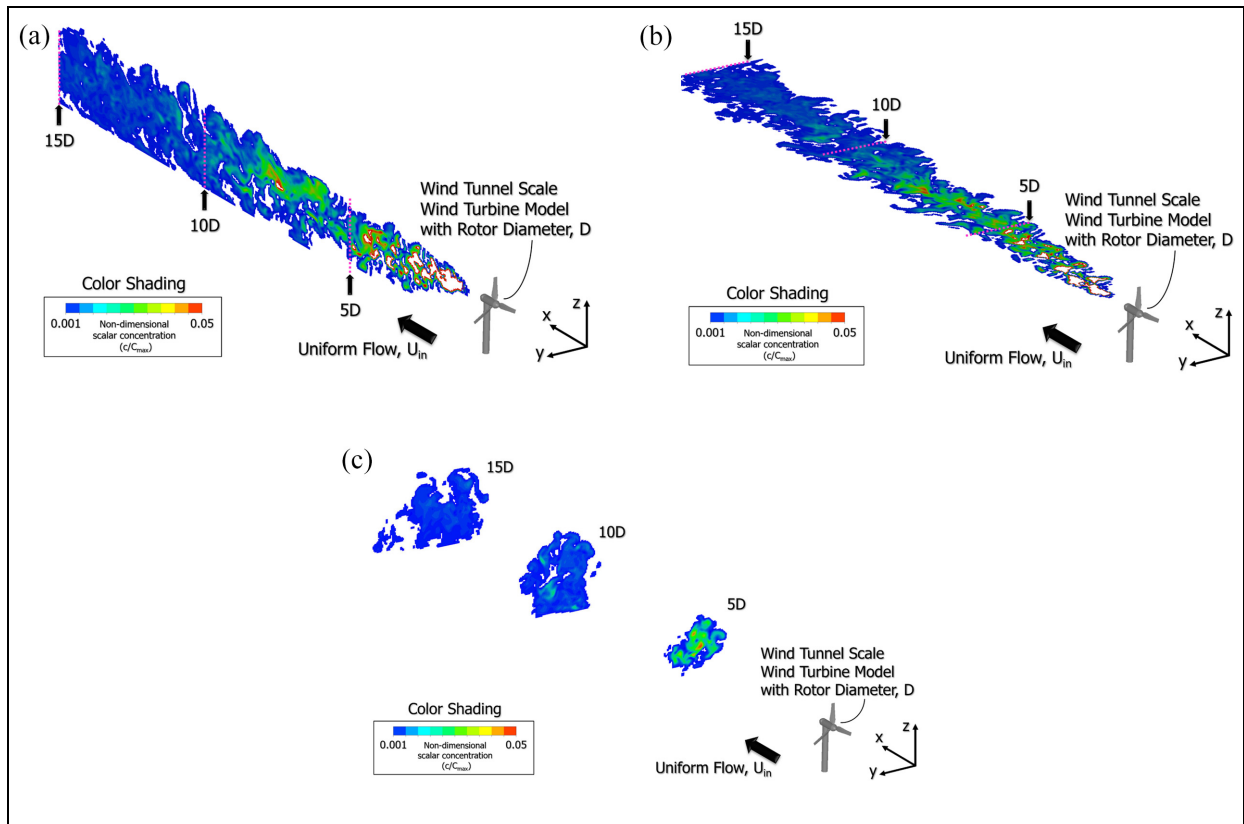


Figure 15. Color shading of non-dimensional instantaneous passive scalar fields released from volume source behind the compact-type small-scale wind turbine model: (a) x - z (side) plane, (b) x - y (top) plane, and (c) y - z (rear) planes.

instantaneous numerical results obtained by the proposed method. Through visual observation of the passive scalar behavior, we considered the complicated three-dimensional structure of the wake flows and clarified the effectiveness of the proposed method. The mixing and transport of passive scalars released continuously into a wake region from the volume source behind the wind turbine model was clearly confirmed, due to wake spreading. The turbulence spreading and dispersion of passive scalars confirmed the smoke behavior in the wind tunnel experiment shown in Figure 11.

Furthermore, in order to investigate whether the overall structure of the wake flow could be realized, a volume source the same size as the swept area was set (as shown in Figure 16), and the numerical results obtained by the proposed method were considered in more detail (see Figures 17 and 18). Figure 17 shows the non-dimensional instantaneous spatial distribution of the stream-wise velocity and passive scalar fields behind the compact-type small-scale wind turbine model. It should be noted here that the color shading indicates the non-dimensional

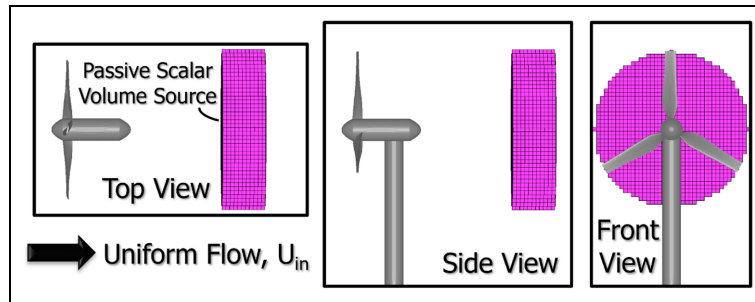


Figure 16. Passive scalar volume source behind the compact-type small-scale wind turbine model, which was disk-shaped and was the same size as the swept area.

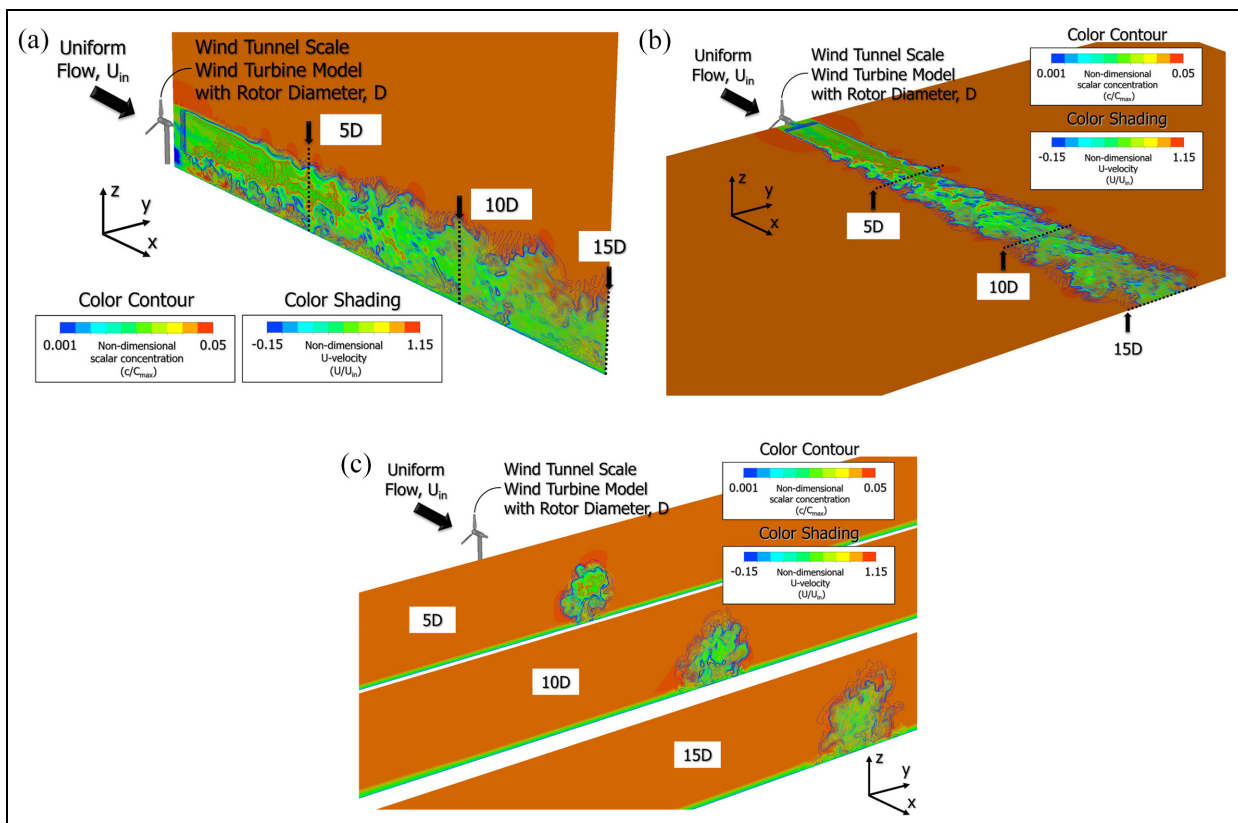


Figure 17. Non-dimensional instantaneous spatial distribution of the stream-wise velocity and passive scalar fields behind the compact-type small-scale wind turbine model: (a) x - z (side) plane, (b) x - y (top) plane, and (c) y - z (rear) planes.

spatial distribution of the stream-wise velocity, while the color contour indicates the non-dimensional spatial distribution of the passive scalar concentration. Figure 18 shows the time-averaged numerical results corresponding to Figure 17. The numerical results indicated that the passive scalars continuously emitted from behind the model were trapped within the wake region and were dispersed. This clarified that the spatial distribution pattern of the color contour of the non-dimensional scalar concentration and the spatial distribution pattern of the color shading of the non-dimensional stream-wise velocity (U -velocity) were similar. Therefore, our proposed numerical method was shown to be effective. From a detailed examination of the results, we concluded that the strong helical-tip vortices played a dominant role, and acted as a barrier preventing momentum exchange between the external and wake flows.

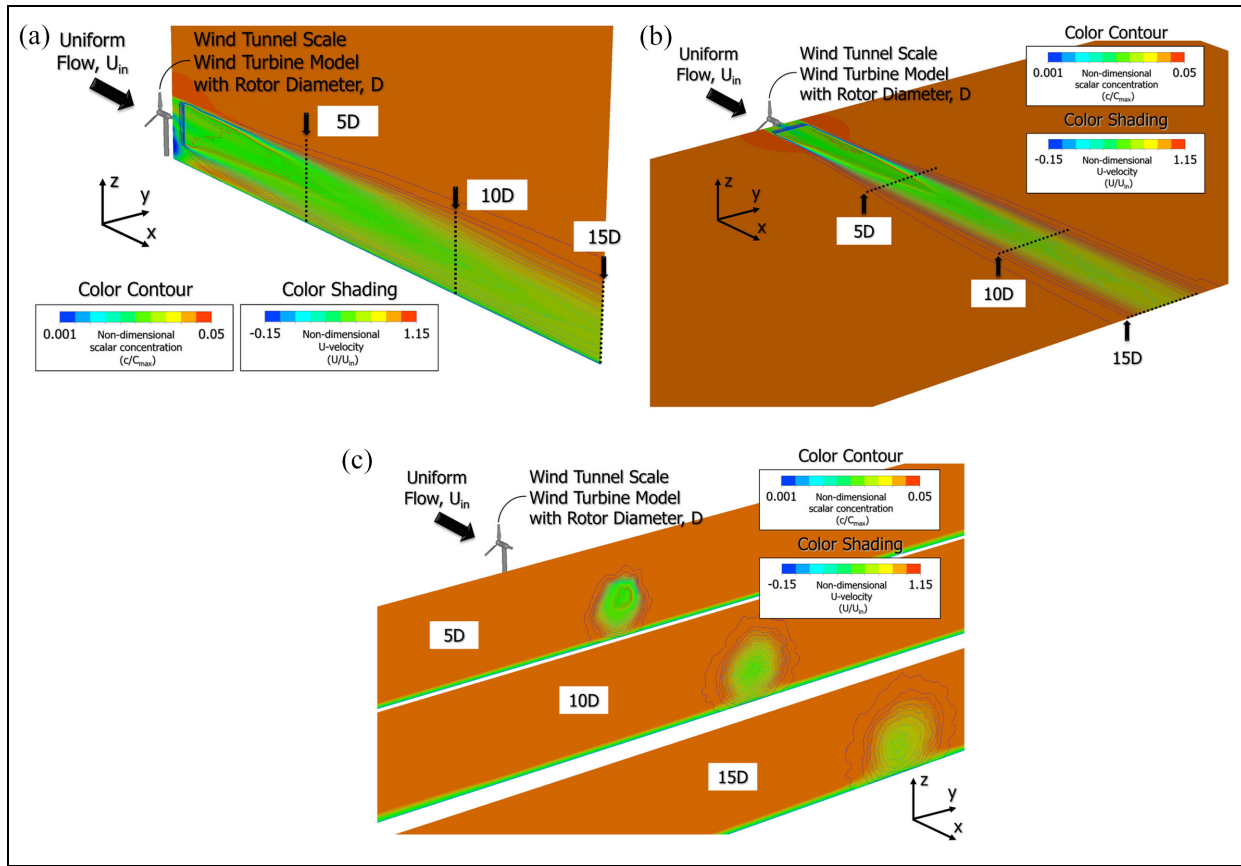


Figure 18. Non-dimensional time-averaged spatial distribution of the stream-wise velocity and passive scalar fields behind the compact-type small-scale wind turbine model: (a) x - z (side) plane, (b) x - y (top) plane, and (c) y - z (rear) planes.

Based on the time-averaged numerical results, the horizontal and the vertical distributions of the non-dimensional stream-wise velocity and non-dimensional passive scalar at three typical positions ($x = 5$, 10 , and 15 D) were extracted; see Figures 19 and 20. The numerical results shown in Figures 19b and 20b were obtained under the assumption that a volume source of the same size as the swept area was set behind the model, and passive scalars were continuously emitted into the wake region. As can be seen from Figures 19a and 20a, a strong velocity shear was formed near the blade tip, due to periodic shedding of the stronger and more stable helical-tip vortex in the near-wake cross-sections ($x = 5$ D). In contrast, in the far-wake regions ($x = 10$ and 15 D), the time-averaged stream-wise velocity deficits in the horizontal x - y and vertical x - z cross-sections approached a Gaussian wake profile, which is axisymmetric and self-similar (Porté-Agel et al., 2020). The shape of the profiles shown in Figures 19b and 20b are similar to those shown in Figures 19a and 20a, despite having opposite signs. This result suggests that, if an appropriate volume source was set behind the wind turbine, the behavior of the wake flow could potentially be predicted by the behavior of the passive scalars continuously emitted from the volume source.

Finally, the proposed method was applied to a large offshore wind farm, consisting of 12 wind turbines. Figure 21 shows the computational domain, grid, and resolutions for the large offshore wind farm. As illustrated in Figure 21, a wind farm configuration with equal row and column spacing ($3D$) was assumed, to clarify the mutual interference phenomenon between the wind turbine wakes. The National Renewable Energy Laboratory (NREL) 5 MW offshore wind turbine, with a rotor diameter of 126 m and a hub height of 92 m, was used. For the simulation, we set the 1/10th power-law mean velocity profile without inflow turbulence. Effects of turbulent inflow conditions on wind turbine performance and wake structure are extremely important issues and will be discussed in the near future. Other initial and boundary conditions were the same as those used for the numerical results above. In addition, two types of simulations were performed, including one where the wind turbine faced the wind and another where the wind turbine was tilted 15° , with respect to the wind.

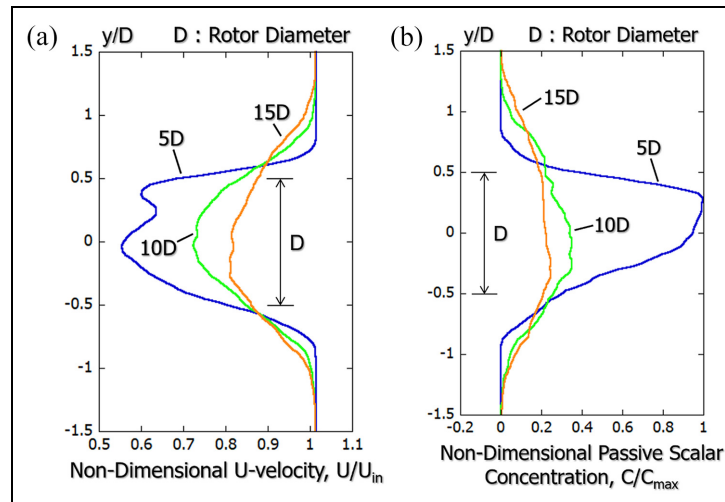


Figure 19. Horizontal distribution at three typical positions ($x = 5, 10,$ and $15 D$): (a) non-dimensional time-averaged stream-wise velocity and (b) non-dimensional time-averaged passive scalar.

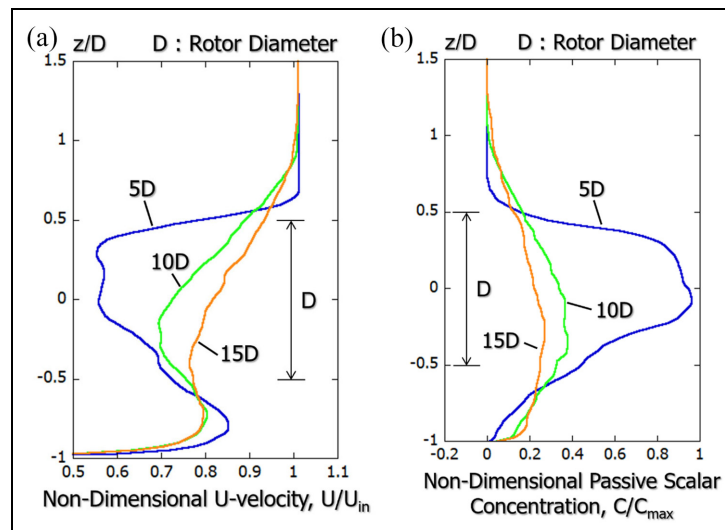


Figure 20. Vertical distribution at three typical positions ($x = 5, 10,$ and $15 D$): (a) non-dimensional time-averaged stream-wise velocity and (b) non-dimensional time-averaged passive scalar.

In this study, we focused on how the wake flow caused by wind turbine 1 interferes with the wake flows of other wind turbines located around it. For that reason, the volume source of the passive scalars was set behind wind turbine 1. The size of the volume source was similar to the swept area of the wind turbine. Figure 22 shows the non-dimensional instantaneous spatial distribution (black and white shading) of the stream-wise velocity and passive scalar fields. First, we focused on the non-dimensional instantaneous spatial distribution of the stream-wise velocity. In both scenarios, the complex interactions between wake flows developed by the wind turbines were reproduced. In Figure 22b, where the wind direction was tilted by 15° , the gap flow (locally accelerated flow) that formed between the wind turbines in the front row approached the wind turbines in the second rows. This numerical result suggests the effectiveness of wake steering. Second, we examined the instantaneous spatial distribution (color contours) of the passive scalars continuously emitted from the volume source set behind wind turbine 1.

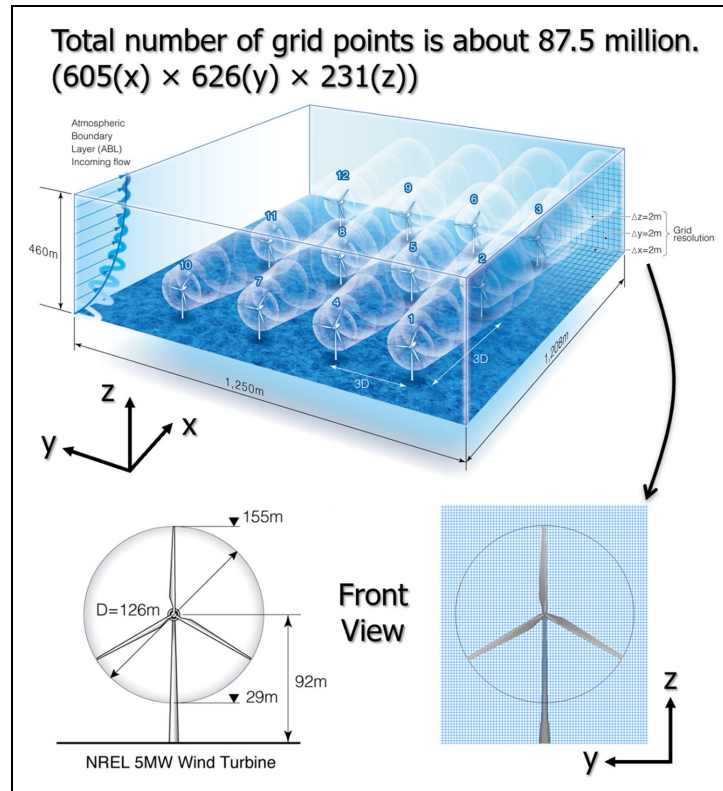


Figure 21. Computational domain, grid, and resolutions, among other aspects, for a large offshore wind farm.

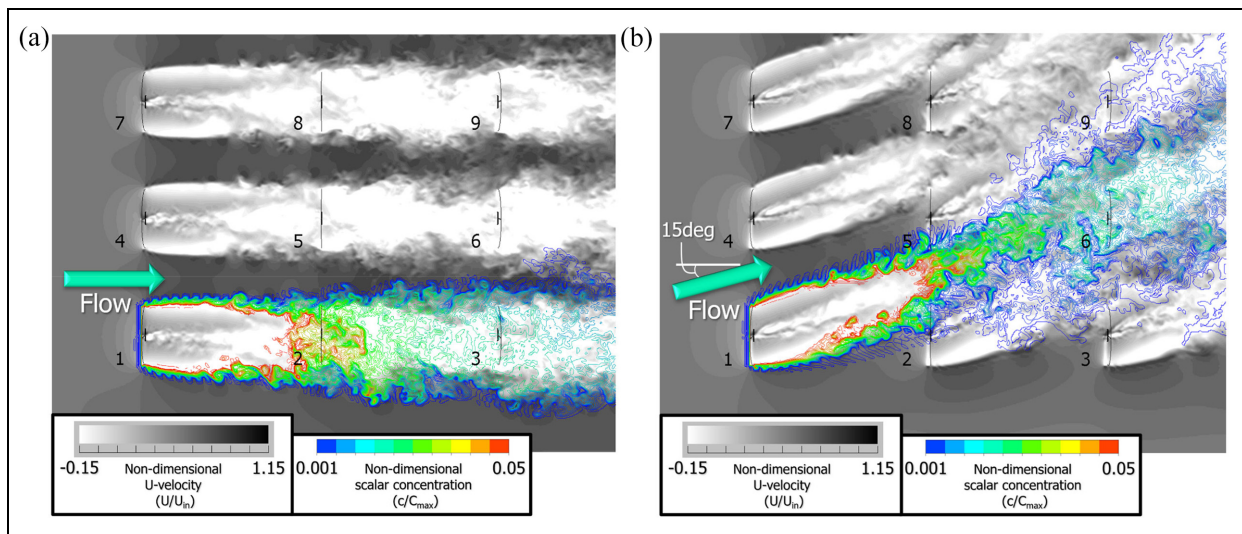


Figure 22. Non-dimensional instantaneous spatial distribution of the stream-wise velocity and passive scalar fields: (a) facing the wind and (b) tilted 15° with respect to the wind.

When comparing the spatial impact of the wake formed by wind turbine 1, we found that the impact was wider, as shown in Figure 22b, than that shown in Figure 22a. Therefore, the proposed numerical method using passive scalars was effective for visually representing the cumulative wake effects in a large, offshore wind farm, due to the effects of the mutual interactions between the wakes on downstream turbines.

Conclusions

In this study, we proposed a novel numerical methodology to visualize and characterize the unsteady properties of wakes trailing behind wind turbines. In a wind-tunnel experiment using a compact-type small-scale wind turbine model, smoke was generated from behind the model to visualize the wake flow; that is, the wind turbine wake could be visualized as a result of the continuous scalar plumes created at a consistent point source. Comparatively, a high-fidelity large-eddy simulation (LES)-based data visualization using a passive scalar advection–diffusion equation was also proposed. The proposed method uses the actuator-line concept for the wind turbine model. We succeeded in qualitatively reproducing the wake visualization experiment in the wind tunnel. Next, a disk-shaped volume source having the same size as the swept area was placed just behind the wind turbine model. Through time-averaged comparisons, it became clear that the non-dimensional time-averaged passive scalar profile in three typical positions ($x = 5, 10, \text{ and } 15 \text{ D}$) closely matched the shape of the stream-wise velocity profile, despite having opposite signs. Finally, in order to validate the proposed method for wake management, we carried out visualization of the wake flows around a virtual offshore wind farm consisting of 12 wind turbines. Through a detailed comparison of two types of numerical results with different wind directions, we found that the proposed method can effectively demonstrate the range of spatial influence of the wakes formed by the wind turbine of interest.

Declaration of conflicting interests

The author(s) declared no potential conflicts of interest with respect to the research, authorship, and/or publication of this article.

Funding

The author(s) disclosed receipt of the following financial support for the research, authorship, and/or publication of this article: A part of this work was supported by KAKENHI (21H01574) and Adaptable and Seamless Technology transfer Program through Target-Driven R&D (A-STEP) from Japan Science and Technology Agency (JST) grant number JPMJTR211C.

ORCID iDs

Takanori Uchida  <https://orcid.org/0000-0003-2630-9113>

Susumu Takakuwa  <https://orcid.org/0000-0003-2086-0078>

References

- Emeis S (2010) Meteorological explanation of wake clouds at horns Rev wind farm. *DEWI-Magazin* 37: 52–55.
- Hasager C, Nygaard N, Volker P, et al. (2017) Wind farm wake: The 2016 horns Rev photo case. *Energies* 10(3): 317–324.
- Houck DR (2022) Review of wake management techniques for wind turbines. *Wind Energy* 25: 195–220.
- Inagaki M, Kondoh T and Nagano Y (2005) A mixed-time-scale SGS model with fixed model-parameters for practical LES. *Journal of Fluids Engineering* 127(1): 1–13.
- Kajishima T (1994) Upstream-shifted interpolation method for numerical simulation of incompressible flows. *Transactions of the Japan Society of Mechanical Engineers Series B* 60: 3319–3326.
- Kawamura T, Takami H and Kuwahara K (1986) Computation of high Reynolds number flow around a circular cylinder with surface roughness. *Fluid Dynamics Research* 1: 145–162.
- Kim J and Moin P (1985) Application of a fractional-step method to incompressible Navier-Stokes equations. *Journal of Computational Physics* 59: 308–323.
- Matsumiya H, Kogaki T, Takahashi N, et al. (2011) Development and experimental verification of the new MEL airfoil series for wind turbines. *Proceedings of Japan Wind Energy Symposium* 22: 92–95.
- Porté-Agel F, Bastankhah M and Shamsoddin S (2020) Wind-turbine and wind-farm flows: A review. *Boundary-Layer Meteorology* 174(1): 1–59.
- Richmond-Navarro G, Uchida T and Calderón-Muñoz WR (2022) Shrouded wind turbine performance in yawed turbulent flow conditions. *Wind Engineering* 46: 518–528.
- Sanderse B, Pijl SP and Koren B (2011) Review of computational fluid dynamics for wind turbine wake aerodynamics. *Wind Energy* 14(7): 799–819.
- Sørensen JN (2011) Instability of helical tip vortices in rotor wakes. *Journal of Fluid Mechanics* 682: 1–4.
- Uchida T (2020) Effects of inflow shear on wake characteristics of wind-turbines over flat terrain. *Energies* 13(14): 3745–3831.
- Uchida T and Araya R (2021) Applications of the atmospheric transport and diffusion of LES modeling to the spread and dissipation of COVID-19 aerosol particles inside and outside the Japan National Stadium (Tokyo Olympic Stadium). *Modelling and Simulation in Engineering* 2021: 1–19.

Uchida T and Li G (2018) Comparison of RANS and LES in the prediction of airflow field over steep complex terrain. *Open Journal of Fluid Dynamics* 8: 286–307.

Vermeer LJ, Sørensen JN and Crespo A (2003) Wind turbine wake aerodynamics. *Progress in Aerospace Sciences* 39: 467–510.

Appendix

Nomenclature

x	streamwise coordinate
y	spanwise coordinate
z	vertical coordinate
\bar{u}	filtered instantaneous streamwise velocity
\bar{v}	filtered instantaneous spanwise velocity
\bar{w}	filtered instantaneous vertical velocity
\bar{p}	filtered instantaneous dynamic pressure
\bar{c}	filtered passive scalar concentration
Re	Reynolds number
Pr	Prandtl number
τ_{ij}	SGS stress (SGS: sub-grid scale)
h_j	SGS scalar flux
ν_{SGS}	SGS eddy viscosity coefficient
α_{SGS}	SGS scalar diffusion coefficient
Pr_{SGS}	SGS Prandtl number
\bar{S}_{ij}	resolvable-scale strain rate tensor
$ \bar{S} $	magnitude of resolvable-scale strain rate tensor
k_{es}	velocity scale squared
T_S	time scale
C_{MTS} C_T	model parameter
Δ	filter length scale